Aerothermodynamic Shape Optimization of Reentry Capsules Using DSMC and POD Methods

H. Kutkan* and S. Eyi*
Corresponding author: halit.kutkan@metu.edu.tr

*Middle East Technical University, TURKEY.

Abstract: This paper presents a hybrid method based on proper orthogonal decomposition (POD) with a trained radial basis function (RBF) network, on direct simulation monte carlo (DSMC) solutions for aerothermodynamic front surface optimization of Stardust re-entry. Gaussian and multiquadric RBFs are implemented for comparison, and multiquadric functions are chosen due to their insensitivity to diverse shape parameters. Cubic uniform B-spline curves are used innovatively for parameterization of the geometry change, instead of curve fitting the geometry itself. This makes possible to reduce the number of design variables. Gradient based optimization strategy is implemented by regarding the distributions of pressure, shear stress and heat flux along the surface of the geometries. G.A. Bird's two dimensional axisymmetric DSMC solver [1] is used as the physics solver, and 11 species air model are chosen with 41 chemical reactions according to atmospheric conditions of the re-entry. Different geometries are obtained via deviating the design variables arbitrarily to form a snapshot pool. In this manner, the approximation success of the POD-RBF methodology is tested on highly nonlinear flow conditions with arbitrarily chosen design of experiment. Finally, the optimized geometries are simulated via DSMC code and the solutions are compared with the solutions of POD-RBF network. Method lowered the optimization time extraordinarily and provided satisfactory results.

Keywords: DSMC, POD, RBF, Hypersonic flow, Optimization.

1   Introduction

Re-entry vehicles are the most common type of hypersonic vehicles. They enter atmosphere at high altitudes where the air is highly rarefied. They are designed for slowing down the velocity by increasing the drag force along their trajectory. However, they are exposed to very high velocities where the highly energetic thermochemical effects are dominant. In addition to this, strong shock waves generate tremendous heat on the windward side. Hence, the design requires accurate prediction of surface quantities such as heat flux, pressure and shear stress to calculate the aerodynamic forces and moments. These properties are not only responsible for the aerodynamic performance of the vehicle, they are also responsible for the selection and the sizing of the thermal protection system (TPS), which protects the vehicle from extreme heating [2].

Literature studies show that the CFD methods based on continuum approach have difficulties for predicting the shock region in hypersonic flows. This is mainly sourced by the effect of aerothermochemical non-equilibrium condition. In this manner, continuum methods are not able to simulate the physical effects that occur at the molecular level [1]. Thus, the DSMC methodology comes into prominence for dealing with this phenomenon because of its particle-based approximation.

Hence it is preferred for simulating the flow field instead of CFD.

Direct Simulation Monte Carlo (DSMC) method was developed by G. A. Bird for simulating directly the physical movements of the molecules in gas flows. It is derived from the Boltzmann Equation through Chapman Enskog approximation and the details of the method can be found from [1, 3]. It has been used in many studies in the field of hypersonic aerothermodynamics [4, 5, 6, 7, 8, 9].

DSMC method is very useful while simulating rarefied gas flows. However, its utilization for optimization study still needs a considerable amount of computation process. To reduce the computation time and dynamize the optimization process, Proper Orthogonal Decomposition (POD) methodology may be used. It can be stated that POD is such a mathematical method that provides an optimally ordered orthonormal basis in the least squares sense for a given set of data [10]. POD can obtain this orthonormal basis either taking singular value decomposition (SVD) [11] of the original data matrix or determining the eigenvector matrix of the covariance matrix [12, 13]. Furthermore, this basis can be used either for reconstruction or extrapolation of the prospective vectors.

POD has been widely used in the field of aerodynamics with linear regression models [11, 12, 13] successfully. However, its usage with linear regression models fails down when the nonlinear flow conditions are dominant. Jing [14] investigated the interpolation and extrapolation capability of POD on NACA 0012 airfoil in transonic conditions with linear regression model and showed the inaccuracy in extrapolation. The reason for this, lies under the evaluation of coefficients of POD basis modes. Linear regression methods like least squares cannot extract the nonlinear system behavior and may cause fallacies especially in the flows where the discontinuities occur. To overcome this situation, nonlinear regression methods such as: quadratic polynomials or neural networks like radial basis functions (RBF) may have been utilized. Having said that, the nonlinear regression examples in the literature have been applied on the continuum approach solutions such as: FEM or CFD [15, 16, 17, 18, 19, 20, 21]. In this sense, the present study may have a place in the literature, for investigating the success of POD with nonlinear regression on particle based stochastic approach solutions.

In the present study, aerothermodynamic front shape optimization of the Stardust reentry has been studied. The atmospheric conditions of trajectory point at 81 km altitude was chosen as the flow conditions due to be the region of continuum breakdown. Innovative parameterization approach has been made via implementing the B-spline curves for fitting the geometry change, instead of the geometry itself. Thus, the number of control points has been able to be decreased. The base Stardust geometry was composed of 600 intervals and the intervals of the cubic B-splines were also held as equal. Varying geometries' coordinate vectors were formed by summing up the cubic B-spline's interval nodes and the base Stardust geometry nodes. Snapshot pool had been composed of 40 arbitrarily chosen geometry solutions initially and it was expanded up to 90 solutions finally, in line with the requirements. Leave-One-Out (LOO) cross validation method [21] was implemented for specifying these requirements. DS2V direct simulation monte carlo code [1] used as the physics solver and reduced order model was developed via trained POD-RBF network [19, 20]. Multiquadric and gaussian RBFs were implemented for comparison, and multiquadric RBFs was chosen for optimization in case of its relative insensitivity to model shape parameter [15, 16]. Gradient based optimization tool DOT [22] was used for optimization. 4 different optimized geometry were obtained at the end of the optimization by changing the objective and the constraint functions. Aerodynamic drag and the total heat energy were calculated by integrating the distribution of pressure, shear stress and heat flux along the surface of the geometries. The optimized geometries were simulated via DS2V after the optimization. Pressure, shear stress and heat flux distributions were plotted and compared with the solutions of reduced order model. Trained POD-RBF network has been found as capable of responding the non-linear characteristics of the system. However, it is found that more comprehensive snapshot pool would be beneficial. Although the prediction accuracy is almost excellent when the prospective geometry is close to the one in the snapshot pool, there might be some discrepancies according to the dissimilarity of prospective geometry.

2 Flow-field Solutions

The freestream conditions of the trajectory point can be found from the available spectral measurements during Stardust entry and are tabulated below [4]. Corresponding Knudsen number of the flow lies in a region where the continuum breakdown occurs. Letting us the comparison of the study with both CFD and DSMC calculations in the literature. The dimensions of the geometry are given in the Figure 1.
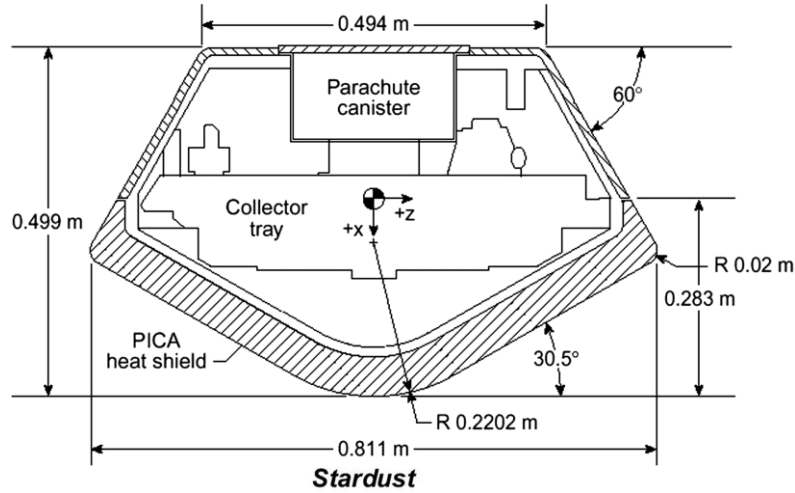

Figure 1: Geometry of the Stardust re-entry [4]

The chosen trajectory point of re-entry and its freestream conditions are tabulated below. (Table 1)

Table 1: Freestream conditions at 81 km altitude [4]

Freestream temp, K	217.6
Freestream number density, molecules/m³	2.64E+20
Freestream velocity, m/s	12385
Freestream O_2 mole fraction %	23.67
Freestream N_2 mole fraction %	76.23
Freestream Knudsen number	0.005

According to the freestream conditions, eleven species real air model was used for including the effects of nonequilibrium aerothermodynamics. The chemical reaction set with 41 equations (Table 2) was used and it was simulated using Total Collision Energy (TCE) [3] model. Recombination of particles (atoms, ions and molecules) in the flow-field and ablation of surface were neglected; however, the dissociation, exchange and ionization reactions were implemented in the calculations. While forebody surface of the reentry was assumed as fully catalytic to recombination of atoms, ions and electrons, the aft body was assumed as noncatalytic. The constant wall temperature of 2000 K was used for the forebody surface and 900 K for the aft body surface.

The implemented set of chemical reactions are given in Table 2.

Table 2: List of chemical reactions [6]

No	Reaction (Energy in J)	Rate Coefficient (m^3/molecule s)
1.	$O_2 + N + 8.197x10^{-19} \rightarrow 2O + N$	$1.375x10^{-10}T^{-1}\exp(-59370/T)$
2.	$O_2 + NO + 8.197x10^{-19} \rightarrow 2O + NO$	$4.58x10^{-11}T^{-1}\exp(-59370/T)$
3.	$O_2 + N_2 + 8.197x10^{-19} \rightarrow 2O + N_2$	$4.58x10^{-11}T^{-1}\exp(-59370/T)$
4.	$2O_2 + 8.197x10^{-19} \rightarrow 2O + O_2$	$4.58x10^{-11}T^{-1}\exp(-59370/T)$
5.	$O_2 + O + 8.197x10^{-19} \rightarrow 3O$	$1.375x10^{-10}T^{-1}\exp(-59370/T)$
6.	$N_2 + O + 1.561x10^{-18} \rightarrow 2N + O$	$1.85x10^{-8}T^{-1.6}exp(-113000/T)$
7.	$N_2 + O_2 + 1.561x10^{-18} \rightarrow 2N + O_2$	$6.17x10^{-9}T^{-1.6}exp(-113000/T)$
8.	$N_2 + NO + 1.561x10^{-18} \rightarrow 2N + NO$	$6.17x10^{-9}T^{-1.6}exp(-113000/T)$
9.	$2N_2 + 1.561x10^{-18} \rightarrow 2N + N_2$	$6.17x10^{-9}T^{-1.6}exp(-113000/T)$
10.	$N_2 + N + 1.561x10^{-18} \rightarrow 3N$	$1.85x10^{-8}T^{-1.6}exp(-113000/T)$
11.	$NO + N_2 + 1.043x10^{-18} \rightarrow N + O + N_2$	$3.83x10^{-13}T^{-0.5}exp(-75550/T)$
12.	$NO + O_2 + 1.043x10^{-18} \rightarrow N + O + O_2$	$3.83x10^{-13}T^{-0.5}exp(-75550/T)$
13.	$NO + NO + 1.043x10^{-18} \rightarrow N + O + NO$	$3.83x10^{-13}T^{-0.5}exp(-75550/T)$
14.	$NO + O + 1.043x10^{-18} \rightarrow N + 2O$	$7.66x10^{-13}T^{-0.5}exp(-75550/T)$
15.	$NO + N + 1.043x10^{-18} \rightarrow 2N + O$	$7.66x10^{-13}T^{-0.5}exp(-75550/T)$
16.	$NO + O + 2.19x10^{-19} \rightarrow N + O_2$	$3.6x10^{-22}T^{1.29}exp(-19700/T)$
17.	$N_2 + O + 5.175x10^{-19} \rightarrow N + NO$	$5.3x10^{-17}T^{0.1}exp(-37500/T)$
18.	$O_2 + N \rightarrow 2.19x10^{-19} + O + NO$	$5.2x10^{-22}T^{1.29}exp(-3600/T)$
19.	$NO + N \rightarrow 5.175x10^{-19} + O + N_2$	$2.02x10^{-17}T^{0.1}$
20.	$N + O + 4.442x10^{-19} \rightarrow NO^+ + e^-$	$2.55x10^{-20}T^{0.37}exp(-32030/T)$
21.	$O + e^- + 2.18x10^{-18} \rightarrow O^+ + 2e^-$	$3.00x10^{-12}exp(-157900/T)$
22.	$O + O + 1.12x10^{-18} \rightarrow O_2^+ + e^-$	$6.42x10^{-22}T^{0.49}exp(-81100/T)$
23.	$O_2^+ + e^- \rightarrow 1.12x10^{-18} + O + O$	$3.83x10^{-9}T^{-1.51}$
24.	$O + O_2^+ + 2.57x10^{-19} \rightarrow O^+ + O_2$	$1.89x10^{-16}T^{-0.52}exp(-18760/T)$
25.	$O^+ + O_2 \rightarrow 2.57x10^{-19} + O + O_2^+$	$1.89x10^{-16}T^{-0.52}$
26.	$N^+ + N_2 + 1.67x10^{-19} \rightarrow N + N_2^+$	$1.67x10^{-17}T^{-0.18}exp(-12100/T)$
27.	$O + NO^+ + 7.04x10^{-19} \rightarrow O^+ + NO$	$4.58x10^{-17}T^{0.01}exp(-51000/T)$
28.	$N + N + 9.34x10^{-19} \rightarrow N_2^+ + e^-$	$2.98x10^{-20}T^{0.77}exp(-67650/T)$
29.	$N + e^- + 2.33x10^{-18} \rightarrow N^+ + 2e^-$	$1.00x10^{-14}exp(-168800/T)$
30.	$O^+ + NO \rightarrow 7.04x10^{-19} + O + N_2^+$	$1.97x10^{-17}T^{0.01}$
31.	$O^+ + N_2 + 3.06x10^{-19} \rightarrow O + N_2^+$	$1.06x10^{-16}T^{-0.21}exp(-22160/T)$
32.	$N_2^+ + e^- \rightarrow 9.34x10^{-19} + N + N$	$8.88x10^{-10}T^{-1.23}$
33.	$NO^+ + e^- \rightarrow 4.42x10^{-19} + N + O$	$4.03x10^{-9}T^{-1.63}$
34.	$N_2^+ + N \rightarrow 1.66x10^{-19} + N^+ + N_2$	$2.37x10^{-18}T^{-0.52}$
35.	$N_2^+ + O \rightarrow 3.15x10^{-19} + O^+ + N_2$	$1.77x10^{-17}T^{-0.21}$
36.	$N + NO^+ + 8.43x10^{-19} \rightarrow N^+ + NO$	$1.84x10^{-15}T^{-0.02}exp(-61060/T)$
37.	$N^+ + NO \rightarrow 8.43x10^{-19} + N + NO^+$	$1.84x10^{-15}T^{-0.02}$
38.	$O_2 + NO^+ + 4.47x10^{-19} \rightarrow NO + O_2^+$	$1.72x10^{-14}T^{-0.17}exp(-32400/T)$
39.	$NO + N^+ \rightarrow 4.47x10^{-19} + NO^+ + N$	$4.47x10^{-15}T^{-0.17}$
40.	$N + NO^+ + 4.9x10^{-19} \rightarrow O + N_2^+$	$2.83x10^{-17}T^{0.4}exp(-35500/T)$
41.	$O + N_2^+ \rightarrow 4.9x10^{-19} + N + NO^+$	$4.1x10^{-18}T^{0.4}$

2.1   Direct Simulation Monte Carlo

DSMC calculations are treated in two dimensional, axisymmetric, steady state conditions. Although the DSMC method is naturally unsteady simulation, steadiness can be accessed by taking time average of the time steps. Simulation tool, DS2V [1] is such a visual interactive DSMC program that is capable of solving steady or unsteady two-dimensional flows either it is plane or axisymmetric. It's source code is also available [1] that means one can develop or change the code on its own. In this study, it was used without making any change.

DS2V, models the intermolecular collisions by utilizing the VHS (variable hard sphere) model [3] which corresponds to viscosity and its relation to temperature in continuum approach. Larsen Borgnakke procedures for translational, rotational and vibrational modes of internal energy were explained in detail in ref [3]. Harmonic oscillator theory is implemented for calculation of the effective number of degrees of freedom.

Based on classical collision theory, the chemical reactions are modeled as bimolecular reactions which are the extended version of the bimolecular collisions. According to theory, any reaction can be expressed as follows, where A, B, C and D represent the different species of particles (molecule, atom, ion, electron, photon, etc.)

$$A + B \leftrightarrow C + D \tag{1}$$

In this way, the rate equation for the species A can be written as below:

$$-\frac{dn_A}{dt} = k_f(T)n_A n_B - k_r(T)n_C n_D \tag{2}$$

where n refers to number densities and k_f and k_r represent the rate constants of forward and reverse reactions respectively. The rate constants are functions of temperature and they are not affected by number density or time terms. Furthermore, the rate of the reaction can be dealt with on the empirical basis, so the equation becomes into the form of modified Arrhenius:

$$k(T) = \Lambda T^{\eta} \exp(-E_a/kT) \tag{3}$$

where Λ and η are constants and E_a is the activation energy of the reaction. However, the equation is the function of thermodynamic temperature and the formulation is macroscopic; hence, the nonequilibrium effects cannot be reflected on the procedure. On the other side, the total cross section σ, which is used in the binary molecular collision process, can be used directly if the reaction takes place in which the internal modes of translational degrees of freedom are fully excited. However, the reactions that are placed on the discrete vibrational energy level require an additional reaction cross section σ_r. Also, the ratio of the two cross sections σ_r/σ gives the probability of the reaction, showing whether the collision is resulted as the elastic collision or the reaction. If the total collision energy is lower than the activation energy, the reaction does not take place and the collision will be resulted as elastic collision. In this manner, the temperature dependent rate coefficients of continuum theory are converted into the collisional energy dependent steric factors which are multiplied with elastic cross section in order to obtain the reactive cross section.

Considering the quasi-equilibrium gas, the reaction rate of molecule A can be expressed as follows:

$$\frac{dn_A}{dt} = -\frac{\sigma_r n_A n_B}{\varepsilon}\left(\frac{8kT}{\pi m_r}\right)^{1/2} exp\left(-\frac{E_a}{kT}\right) \tag{4}$$

where ε refers to symmetry factor and it takes the value of 1 for $A \neq B$ and 2 for $A = B$. Comparing Eqn. 3 and Eqn. 4, shows the both are in the same form of the modified Arrhenius equation.

Termolecular reactions have three body collisions and they come into focus when the temperature of the flow field is high enough for dissociation and recombination reactions. A typical reaction can be defined as follows:

$$AB + T \leftrightarrow A + B + T \tag{5}$$

In the Eqn. 5 AB represents the diatomic or polyatomic molecule and T is the third body molecule. According to AB molecule (diatomic or polyatomic), A and B can be both atom or molecule. Dissociation reactions are endothermic reactions so that the energy E_d is required for occurrence of

the reaction. On the other hand, although the recombination of the *A* and *B* species seem to be a bimolecular reaction regardless of the third body molecule, in order to satisfy the conservation of momentum and the energy equations, the third body molecule is needed for the presence of heat release [3].

The formation and loss of *A* molecule/atom can be expressed as follows for forward and reverse reactions respectively:

$$\frac{dn_A}{dt} = k_f n_{AB} n_T \tag{6}$$

$$\frac{dn_A}{dt} = k_r n_A n_B n_T \tag{7}$$

Similarly, the same equations can be used for finding the rates of species *B*. As it can be understood from the equations, the probability of the recombination reaction is directly proportional to the number density of the third body molecule.

2.2   Validation

Before going into optimization, the flow field solution of Stardust body has been compared with analogous CFD and DSMC studies [4]. Noting that, in molecular regime, quantized temperatures are the measures of the translational and internal (rotational, vibrational and electronical) energies associated with the molecules. Considering temperature as the measure of energy in all flow regimes, translational temperature is assumed as the measure of kinetic energy associated with thermal velocities while the rotational, vibrational and electronical temperatures are associated with the internal energies [1]. To this end, translational temperature was regarded rather than temperature on the contour graphs.
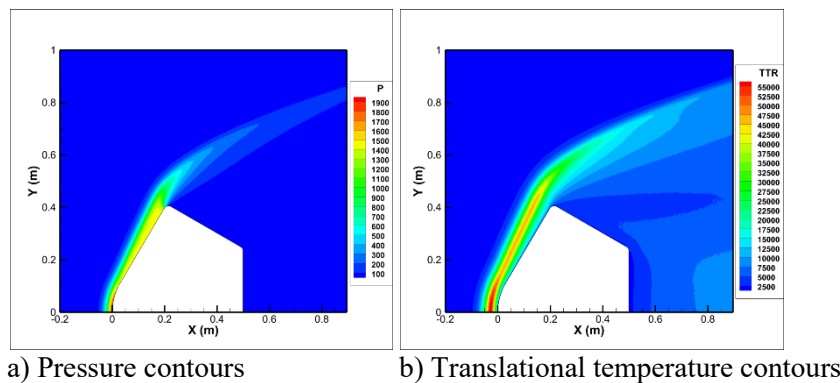

a) Pressure contours   b) Translational temperature contours
Figure 2: Contour plots of Stardust

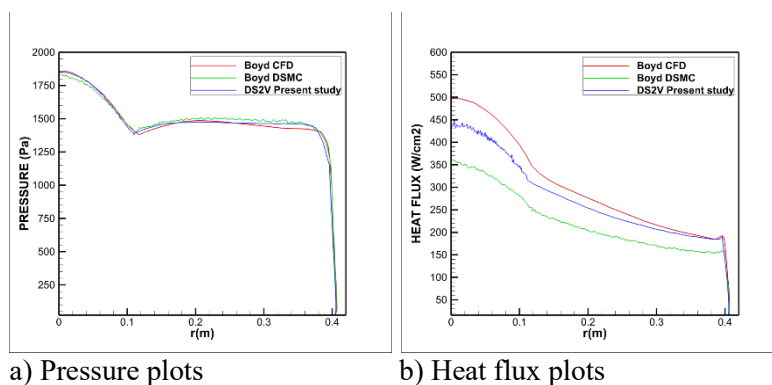a) Pressure plots   b) Heat flux plots
Figure 3: Comparison of pressure and heat flux distributions [4]

Figure 2 shows the pressure and translational temperature contours of the flow field around Stardust re-entry, and Figure 3 shows the comparison of pressure and heat flux distributions which will be used to calculate drag and heat energy soon. Comparison was made both with the results of

CFD and DSMC solutions of [4]. As seen from them, very good agreement was achieved on pressure distributions, and heat flux distributions lie on the averaged line of the ref's [4] DSMC and CFD solutions. Thus, these results have been found as sufficient to continue the optimization process.

3   B-spline Parameterization

Mathematical representation of a curve with control points is provided with the interpolation or approximation scheme which establish the relation between curve and the polygon [23]. Basis functions make the interpolation scheme available. There are several types of basis functions that can be used for representation of curves.

In this study, B-spline basis was chosen for the parameterization process due to its nonglobal behavior. Simply, it allows for defining the order of the curve independently from the number of control points. Any control point affects only the number of neighbor control points which is proportional to the order of the curve, rather than affecting the whole curve.

Considering P(t) as the position vectors along the curve, B-spline curve can be expressed as follows:

$$P(t) = \sum_{i=1}^{n+1} B_i N_{i,k}(t) \qquad t_{min} \leq t < t_{max}, \quad 2 \leq k \leq n+1 \tag{8}$$

where B_i are the position vectors of the $n+1$ defining polygon vertices and $N_{i,k}$ are the normalized B-spline basis functions.

For the ith normalized B-spline basis function of order k (degree $k-1$), the basis functions $N_{i,k}(t)$ are defined by the Cox-deBoor recursion formulas [23]:

$$N_{i,1}(t) = \begin{cases} 1 \ if \ x_i \leq t < x_{i+1} \\ 0 \qquad otherwise \end{cases} \tag{9}$$

and

$$N_{i,k}(t) = \frac{(t - x_i)N_{i,k-1}(t)}{x_{i+k-1} - x_i} + \frac{(x_{i+k} - t)N_{i+1,k-1}(t)}{x_{i+k} - x_{i+1}} \tag{10}$$

Formally the B-spline curve is defined as the polynomial spline function of order k (degree $k-1$), and the function $P(t)$ is a polynomial of degree $k-1$ on each interval $x_i \leq t < x_{i+1}$. $P(t)$ and its derivatives of order $1,2, ..., k-2$ are all continuous over the entire curve.

The above expressions are those that can be used for constituting any B-spline curve. In consideration of parameterization requires an appropriate curve-fitting algorithm. In the same ref. [23], the algorithm was given too. However, the usage of curve fitting algorithm may not always be useful especially where the number of control points is expected to be lower than it must be. In this study, it was aimed to reduce the number of control points without defeating the geometry. So, the B-spline curves were implemented innovatively by parameterizing of geometry change, rather than fitting the geometry itself. Thus, the requirement of curve fitting algorithm was disappeared, and the parameterization could be done with desired number of control points.
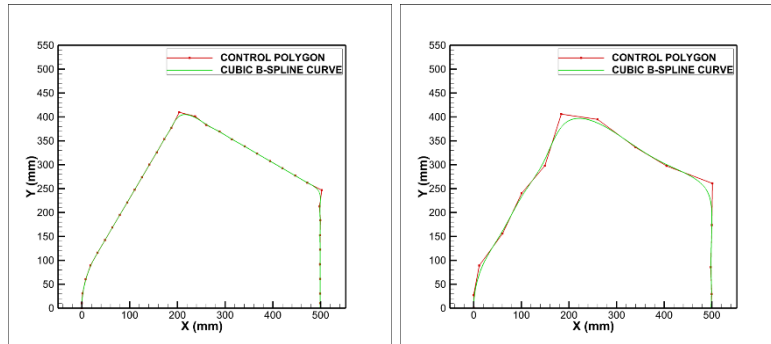
a) with 37 control points   b) with 15 control points

Figure 4: Stardust re-entry geometry curve fitting

As shown in the Figure 4, representing the Stardust geometry via cubic B-splines requires at least of 37 control points by using the curve fitting technique in ref [23]. If we want to represent the same geometry with 15 control points the approximation accuracy decreases badly. However, if the geometry change is parameterized, the number of control points can be specified as much as we desire. In this study, 15 control points were chosen for parameterization in total, and the details of the technique may be explained better on images below.
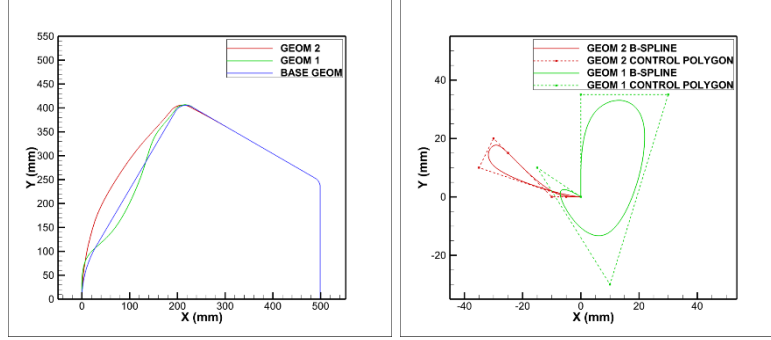
a) Base and resulting geometries b) Control polygons and cubic B-spline curves
Figure 5: Obtained geometries via parameterization of geometry change

First of all, the technique needs a base geometry, which was chosen as Stardust geometry for our study, and an individual B-spline curve. Considering both as two individual curves, their intervals' coordinate points are written in vectorial form and then summed up to form another geometry vector. The major point is to hold the number of intervals identical (or dimension of vectors) on both curves. In this manner, if we want to obtain the same of the base geometry, the control points' coordinates or in other words cubic spline's coordinates are filled with zeros. In Figure 5 b, there are only five control points that can be seen, this is because of the rest of the control points are zero. Therefore, the geometries on the Figure 5 a, were obtained by changing the coordinates of only the five control points.

4   POD-RBF Network

Considering M as the number of snapshots and N as the number of intervals holding the flow variable (pressure, shear stress or heat flux), each snapshot can be written in vectorial form with dimension N. Moreover, these vectors are written as the columns of data matrix U with dimension of NxM. After forming the data matrix, the POD procedure can be followed through two ways for calculating the orthogonal basis. One of them is taking the singular value decomposition (SVD) of the matrix [15, 16, 17, 21], and the second way is evaluating the eigenvector matrix of the covariance or correlation matrix [12, 13, 18, 19, 20]. Second way is followed in this study [19, 20]. Assigning $C=U^T U$ as covariance matrix, nontrivial solution of eigenvalue problem will be the first step as expressed below.

$$C\,V\,=\,\varLambda\,V \qquad\qquad (11)$$

where $\varLambda$ is the diagonal matrix holding the eigenvalues λ_i on its diagonal and V is the eigenvector matrix holding the eigenvectors as its column vectors. From now on the orthogonal POD basis $\varPhi$ can be easily computed via the Eqn. 12.

$$\varPhi\,=\,U\,V\varLambda^{-1/2} \qquad\qquad (12)$$

This POD basis can be truncated to K number of columns where $K < M$ and the resulting matrix is shown as:

$$\widehat{\varPhi}\,=\,U\,\widehat{V}\varLambda^{-1/2} \qquad\qquad (13)$$

In the above expression, $\widehat{\varPhi}$ and $\widehat{V}$ include the first K columns of the relevant matrices. And the number K can be evaluated as holding below expression close to unity.

$$\frac{\sum_{i=1}^{K} \lambda_i}{\sum_{i=1}^{M} \lambda_i} \tag{14}$$

The obtained POD basis either original or the truncated one, both must be orthogonal and provide the orthogonality condition $\Phi^T \Phi = I$, and $\widehat{\Phi}^T \widehat{\Phi} = I$.

Once the truncated POD basis $\widehat{\Phi}$ is computed, the snapshot matrix can be reconstructed or approximated according to the usage of Φ or $\widehat{\Phi}$ respectively.

$$\widetilde{U} = \widehat{\Phi} A \tag{15}$$

In the above expression A refers to the amplitude matrix, and it can be calculated for reconstruction of U or approximation of U as $\widetilde{U}$ through the expression below:

$$A = \widehat{\Phi}^T U \tag{16}$$

If K is chosen equal to M, then the $\widehat{\Phi}$ is automatically changed with Φ in both Eqns. 15 and 16 and $\widetilde{U}$ is also changed with U automatically. Since $\widehat{\Phi}$ is the truncated version of Φ matrix in terms of cancelling the column vectors beyond the Kth column.

Up to now, Sirovich's [24] method of snapshots has been explained. From now on, the following work depends on the study. If the method is used for computing the vector whose parameter is lying between the parameters of two individual solution vectors (e.g. angle of attack dependent airfoil solutions) which are present in the data matrix, POD with interpolation methodology may be used [13]. On the other hand, if the method is used for inverse design problems, gappy POD [12] methodology may be used. These examples can be reproduced according to the goals of the study. However, despite the success of the mentioned methods on continuous flow problems, they cannot produce satisfying results on [14] discontinuous flows such as supersonic and hypersonic, because of implementing linear regression methods. Consequently, in the present study, POD procedure is coupled with radial basis functions (RBF) for reflecting the nonlinear behavior of the system.

The readers who are interested in the theory of the radial basis function (RBF), may find it in detail from [25]. The implementation strategy is explained in the present study. Following from the Eqn. 16, the amplitude matrix A is defined as nonlinear function of the parameter vector [19].

$$A = B F \tag{17}$$

where F denotes the interpolation matrix, and B denotes the coefficient matrix that must be evaluated.

$$F = \begin{bmatrix} f_1(\|\vec{p}_1 - \vec{p}_1\|) & \cdots & f_1(\|\vec{p}_j - \vec{p}_1\|) & \cdots & f_1(\|\vec{p}_M - \vec{p}_1\|) \\ \vdots & & \vdots & & \vdots \\ f_i(\|\vec{p}_1 - \vec{p}_i\|) & \cdots & f_i(\|\vec{p}_j - \vec{p}_i\|) & \cdots & f_i(\|\vec{p}_M - \vec{p}_i\|) \\ \vdots & & \vdots & & \vdots \\ f_M(\|\vec{p}_1 - \vec{p}_M\|) & \cdots & f_M(\|\vec{p}_j - \vec{p}_M\|) & \cdots & f_M(\|\vec{p}_M - \vec{p}_M\|) \end{bmatrix} \tag{18}$$

In Eqn. 18 $\vec{p}_i$ and $\vec{p}_j$ refer to the parameter vectors holding the control point coordinates belong to i^{th} and j^{th} snapshots in the snapshot pool. The $\|\vec{p}_j - \vec{p}_i\|$ corresponds the Euclidian distance between parameter vectors, and $f_i()$ denotes the interpolation function or the radial basis function. By multiplying both sides of Eqn. 17 with F^{-1}, the coefficient matrix B can easily be calculated.

$$B = A F^{-1} \tag{19}$$

Bearing in mind that, the amplitude and the coefficient matrices are known at the moment, from now on equating Eqns. 16 and 17 yields,

$$\widehat{\Phi}^T U = B F \tag{20}$$

Finally, using the orthogonality of $\widehat{\Phi}$, the snapshot matrix U, can be approximated.

$$\widetilde{U} = \widehat{\Phi} B F \tag{21}$$

In the last equation, if Φ is used instead of $\widehat{\Phi}$, then the original U matrix is obtained instead of its approximation matrix $\widetilde{U}$. The Eqn. 21 gives the approximation or the reconstruction of original data matrix (snapshot matrix). However, we need a vector refers to the response solution of prospective design parameters, thus the solution would be in the shape of below,

$$\vec{u}(\vec{p}_{exp}) = \widehat{\Phi} B \vec{f}(\vec{p}_{exp}) \tag{22}$$

Eqn. 22 gives the solution vector, and the model can now be referred as trained POD-RBF network [19, 20]. $\vec{p}_{exp}$ corresponds to the parameter vector of prospective geometry and $\vec{f}(\vec{p}_{exp})$ is the interpolation function vector and can be evaluated via Eqn. 23.

$$\vec{f}(\vec{p}_{exp}) = \begin{Bmatrix} f_1(\|\vec{p}_{exp} - \vec{p}_1\|) \\ \vdots \\ f_i(\|\vec{p}_{exp} - \vec{p}_i\|) \\ \vdots \\ f_M(\|\vec{p}_{exp} - \vec{p}_M\|) \end{Bmatrix} \tag{23}$$

As stated before, two kinds of radial basis functions were implemented and compared, these functions are the Gaussian (Eqn. 24) and multiquadric (Eqn. 25) radial basis functions.

$$f(r) = \exp(-cr^2) \tag{24}$$
$$f(r) = \sqrt{r^2 + c^2} \tag{25}$$

In the above equations, r denotes the Euclidian distance between parameter vectors, and c denotes the model parameter or smoothing factor. In gaussian RBF, c value must be optimized while it takes any value from 0 to 1 in multiquadric RBF. For seeing the interpolation performance of the two RBFs, they were implemented in the trained POD-RBF network and their approximation capability were tested on two arbitrarily chosen geometries from the snapshot pool. Leave one out approach (LOO) [21] was chosen for comparison, since it does not need any extra solutions. In LOO the chosen solutions are taken from the snapshot pool, and they are tried to be extrapolated via the rest of the solutions. Comparison plots of sample 45 and sample 75 are given below:

| a) Sample 45 heat flux | b) Sample 45 pressure | c) Sample 45 shear stress |

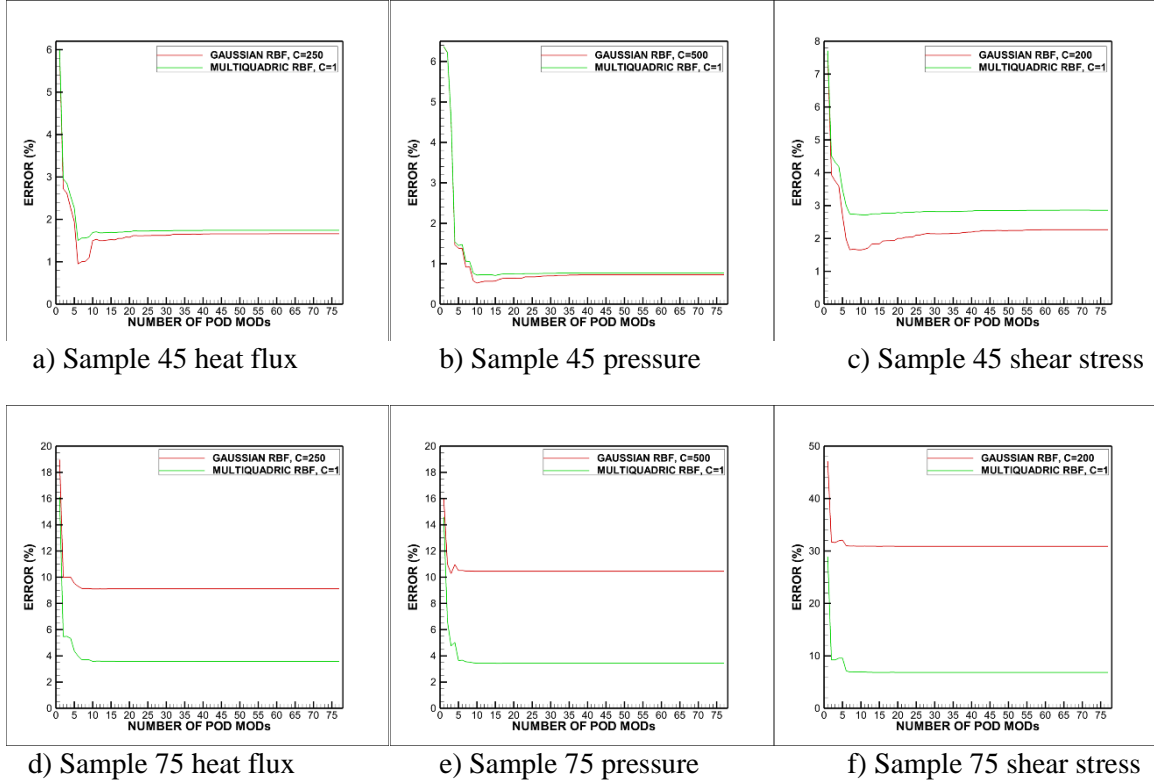| d) Sample 75 heat flux | e) Sample 75 pressure | f) Sample 75 shear stress |

Figure 6: Error charts of gaussian and multiquadric RBFs on sample 45 and sample 75 extrapolation

Percentage errors on the ordinates of Figure 6 a to f were evaluated according to the equation below:

$$\%error = \frac{\|\vec{x}_{app} - \vec{x}\|}{\|\vec{x}\|} \, 100 \tag{26}$$

Figure 6 a, b and c shows the error percentage in the approximation of heat flux, pressure and shear stress distributions along the surface of sample 45. Noting that the model parameter c was

optimized for gaussian RBF by trial and error, and as a value of 1 was used for multiquadric RBF on sample 45 approximation. And the optimized c values were written on the graph's legends. On the other hand, the same optimized values of c were used in the approximation of sample 75. Bearing in mind that and looking at the Figure 6 a to e, if the parameter c is optimized for each of the extrapolation, gaussian RBF can provide more accurate predictions than the multiquadric RBF. However, if they are not optimized the percentage error can increase up to the range of %30's. To this respect, multiquadric RBF were chosen instead of gaussian RBF for its stable error characteristics.

5   Optimization Process

Generally, an optimization problem can be summarized as follows, minimizing or maximizing the objective function subject to constraint function [26]:

$$F[\widehat{W}(D_i), X(D_i), D_i] \qquad (i = 1, \dots \dots I) \qquad (27)$$

$$G_j[\widehat{W}(D_i), X(D_i), D_i] \qquad (j = 1, \dots \dots J) \qquad (28)$$

In the functions, $F, G, \widehat{W}, X, D, I \ and \ J$ are the objective and the constraint functions, state or flow variables, grid coordinates, design variables, numbers of design variables and constraint functions, respectively. The process starts with an initial guess of the design variables, then the design is updated using an iterative procedure:

$$D^k = D^{k-1} + \beta^k S^k \qquad (29)$$

where k refers to the iteration number and the vector S is the search direction and the scalar β is the step size. The optimum step size is found using a one-dimensional search and interpolation. The process is iterated until it converges. The search direction must be both usable and feasible. While usable direction decreases or increases the objective function, feasible direction satisfies the jth constraint.

$$\nabla F(D) \ S \leq 0 \qquad \qquad \nabla G_j(D) \ S \leq 0 \qquad (30)$$

In this study, Stardust's front face optimization has been conducted, considering drag force, maximum heat flux value, total heating energy and volume of the re-entry. These four functions were specified initially and assigning them as objective and constraint functions varyingly, various optimization cases were obtained. Stardust geometry was defined as the base initial geometry and various geometries were produced with B-spline subroutine.

As stated in the section 3, B-spline subroutine had been written as producing the geometries by means of geometry change. So, the required base geometry coordinates were read as an input vector to the subroutine (Figure 7). After reading base geometry vector, it produces geometry according to the geometry parameters (B-spline control points) that come from EVAL subroutine.
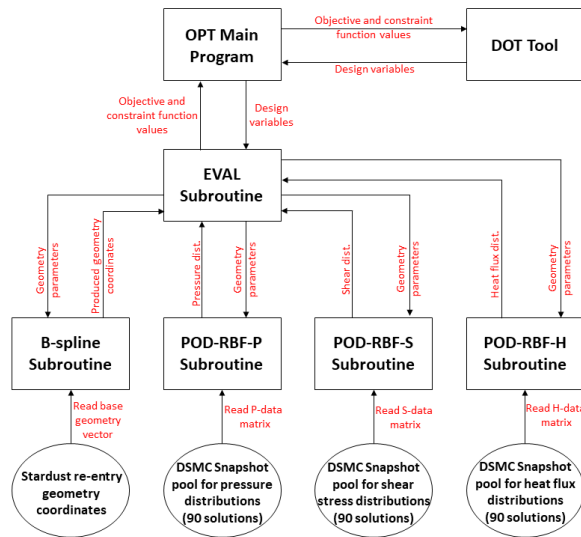

Figure 7: Optimization scheme

EVAL subroutine works as the manager of the optimization (Figure 7). It evaluates the volume of the re-entry geometry by integrating the geometry coordinates from B-spline subroutine. Furthermore, it receives the pressure, shear stress and heat flux distributions from POD-RBF-P, POD-RBF-S and POD-RBF-H subroutines respectively and integrates these distributions over the surface of the geometry for calculating the total values of pressure, shear stress and heat energy. It evaluates the drag force by summing up the total pressure and total shear stress. Also, it evaluates the maximum value of heat flux. Thus, the all of the pre-defined functions such as: total drag, total heating energy, maximum heat flux value and volume of geometry are evaluated and are sent to OPT program for the next step.

OPT program takes these values and transfers to DOT tool and takes the information of next step. The mentioned information holds the geometry parameters of new geometry in terms of design variables. Noting that, design variables are composed of specified number of B-spline control points. However, the geometry parameters in Figure 7 contain the all of 15 B-spline control points. As stated in the section 3 the parameterization had been made by total of 15 control points. On the other hand, as being design variables, 7 control points corresponding to the front face of re-entry were chosen out of 15 control points. Due to this, design variables and geometry parameters were defined separately. In this manner, 7 of the geometry parameters were defined from the design variables, and the rest of them were assigned as zeros.

DSMC snapshot pools were composed of 90 different geometries' DS2V simulations. Since the flow field solutions are not required, they contain the surface distributions of pressure, shear stress and heat flux. Each distribution solution is defined as column vector and they compose matrix together. These matrices are read from POD-RBF subroutines.

6   Results and Discussion

Optimization studies were conducted on four cases such as: maximizing drag force, minimizing heating energy, minimizing maximum heat flux and maximizing the volume. These four objectives were used as constraints also, by leaving alone the objective function. In other words, for the first case, while maximization of drag was the objective function, heat energy, maximum heat flux and the volume were implemented as constraints. Constraints' limit values were held as equal to Stardust's values and side constraints were implemented for constraining the region of design variables.

In all the cases, the front surface of the body was aimed to be optimized so the 7 control points out of total 15 control points were defined as the design variables. These 7 points are those that are responsible for the shape of the front surface. All the cases were initialized from the base Stardust geometry. Additionally, the maximum diameter of the geometry and the location were bounded in a tight space in terms of side constraints, by restricting significant changes in the shape due to the concerns of the snapshot pool scope. When the all four optimized geometries were obtained, they were simulated with DS2V for validation and the results were plotted for comparison.

6.1   Optimized Geometry Solutions Validation

Optimized geometries and their flow variable distributions were given in figures (Figure 8 to Figure 11). The plots contain the DS2V results also for seeing the extrapolation capability of POD-RBF. Additionally, comparative integrated values were expressed in tabulated form in Table 3 to Table 6. Noting that, DS2V flow variable distribution results were filtered via MATLAB's curve fitting tool before taking their integrations due to noise. This procedure was not required for ROM solutions since they are not noisy. For information, filtration process was indicated on the tables.

Table 3: Validation of case 1 maximizing drag on tabulated results (Opt. Geom. 1)

METHOD	PRES. FORCE (N)	SHEAR FORCE (N)	TOT. DRAG FORCE (N)	MAX. HEAT FLUX (W/m²)	TOT. HEAT ENERGY (W)	VOLUME (m³)
POD-RBF	782.48	44.10	826.58	4035206	1376951	0.14483
DS2Vfiltered	774.20	36.49	810.69	4050300	1273461	0.14483
% ERROR	1.07	20.86	1.96	0.37	8.13	-

a) Optimized geometry   b) Heat flux distribution validation

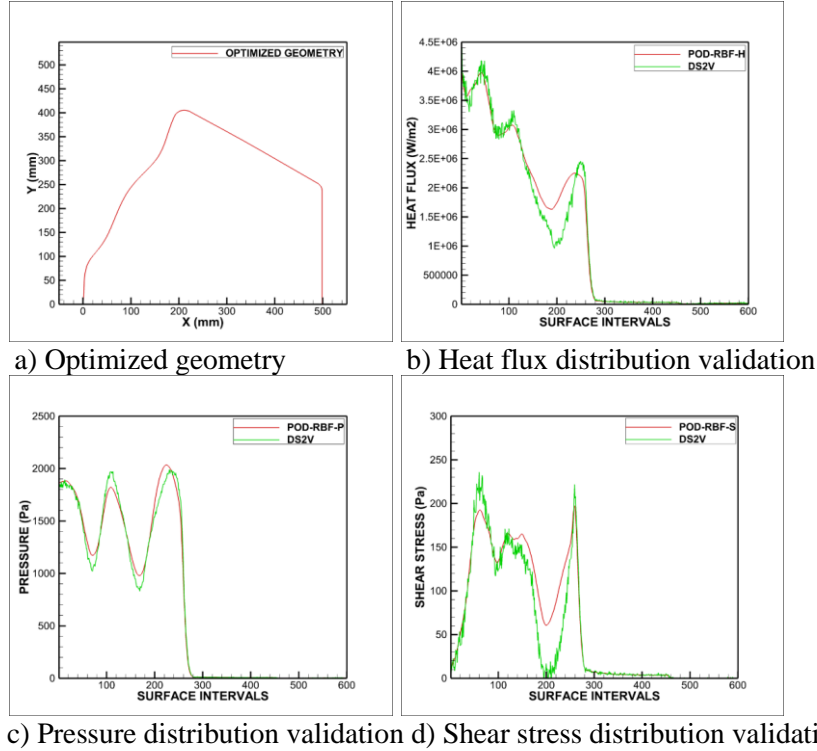c) Pressure distribution validation d) Shear stress distribution validation
Figure 8: Case 1 maximizing drag optimization results validation (Opt. geom. 1)

For the first case, total drag force was defined as objective function to be maximized. On the other hand, volume, maximum heat flux and total heating energy values were defined as constraints, and the Stardust re-entry's values were assigned to these constraints. Figure 8 shows the optimization results in terms of optimized geometry and comparative flow variable distributions over the surface. And Table 3 shows the integrated values in comparison.

According to Figure 8 b heat flux distribution plot, very good agreement was achieved at the region from nose to mid front face. Supporting this agreement, the error percentage in maximum heat flux value was found as 0.37 % (Table 3). However, the agreement starts deviation while approaching to shoulder. And this inconsistency results the error percentage in total heating energy reach up to 8.13 % (Table 3).

On the other hand, very good agreement was able to be achieved in the pressure distribution in Figure 8 c and the error percentage was found as 1.07 % in pressure force (Table 3). Additionally, good agreement was achieved in shear stress distribution except the region between 150th and 250th intervals of surface (Figure 8 d). This region corresponds to the same shoulder region where the disagreement of heat flux distribution is present (Figure 8 b). However, this region affects the integrated value of shear stress more than the integration of heat flux. Shear stress's very low numerical values relative to heat flux, is responsible for the bigger error percentages in comparison (Table 3). Nevertheless, this situation is compensated with adding pressure force while evaluating the total drag force (Table 3).

Table 4 Validation of case 2 minimizing heat energy on tabulated results (Opt. Geom. 2)

METHOD	PRES. FORCE (N)	SHEAR FORCE (N)	TOT. DRAG FORCE (N)	MAX. HEAT FLUX (W/m²)	TOT. HEAT ENERGY (W)	VOLUME (m³)
POD-RBF	736.96	37.75	774.71	4314062	1243186	0.14561
DS2Vfiltered	738.43	37.75	776.19	4316500	1245550	0.14561
% ERROR	0.20	0.01	0.19	0.06	0.19	-

a) Optimized geometry   b) Heat flux distribution validation

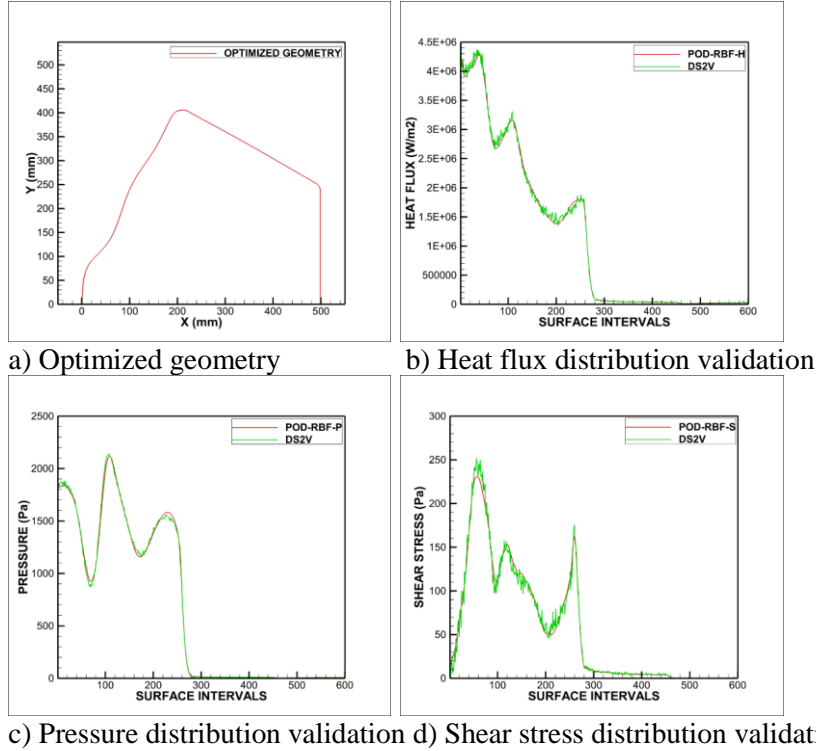c) Pressure distribution validation d) Shear stress distribution validation

Figure 9: Case 2 minimizing heat energy optimization results validation (Opt. Geom. 2)

In this second case, total heating energy was defined as objective function to be minimized. And volume, maximum heat flux and total drag values were defined as constraints, and the Stardust re-entry's values were assigned to these constraints.

According to Figure 9 b, c and d and Table 4, excellent agreement was achieved between DS2V and POD-RBF model. And the results consistency can be seen without the requirement of comment. Interpretations may be made on why the same consistency had not been able to be achieved in the first optimization case while the both optimized geometries look similar (Figure 8 a and Figure 9 a). This may be explained through the conditions which ROM's accuracy is dependent.

Remembering that, the approximation accuracy of ROMs had been dependent on the scope of the snapshot pool and on the uniqueness of the samples. However, any well accepted method was not implemented in this study while forming the solution pool, and the sampling was made arbitrarily. Possibly, relatively more concave region (just before the shoulder) of opt. geom. 1, takes its geometry parameters out of the scope of the snapshot pool and this reduces the approximation accuracy.

Table 5: Validation of case 3 minimizing maximum heat flux on tabulated results (Opt. Geom. 3)

METHOD	PRES. FORCE (N)	SHEAR FORCE (N)	TOT. DRAG FORCE (N)	MAX. HEAT FLUX (W/m²)	TOT. HEAT ENERGY (W)	VOLUME (m³)
POD-RBF	728.28	48.78	777.07	3618034	1376139	0.14532
DS2Vfiltered	719.18	47.19	766.37	3680700	1358001	0.14532
% ERROR	1.27	3.37	1.40	1.70	1.34	-

a) Optimized geometry

b) Heat flux distribution validation

c) Pressure distribution validation d) Shear stress distribution validation
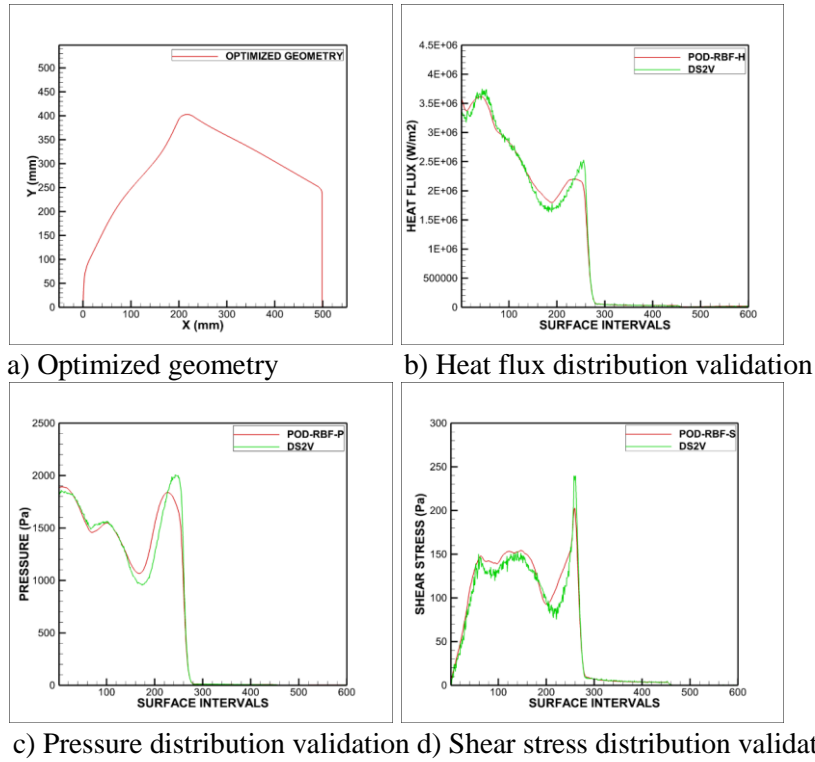
Figure 10: Case 3 minimizing maximum heat flux optimization results validation (Opt. Geom. 3)
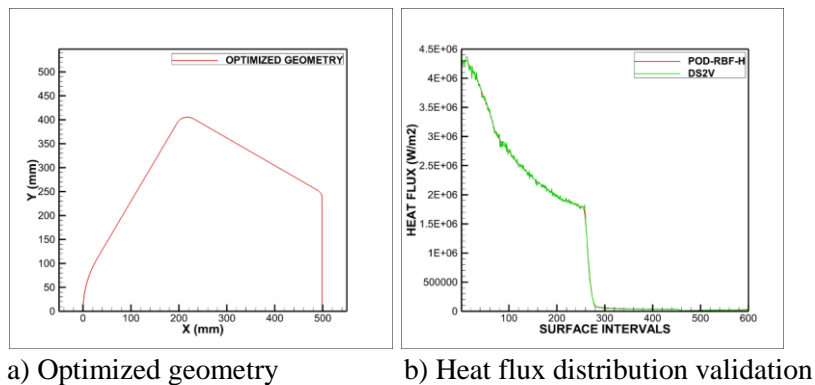
In the third case, objective function was changed to minimization of the maximum heat flux. And volume, total heating energy and total drag values were defined as constraints, and the Stardust re-entry's values were assigned to these constraints.

By looking at Figure 10, almost very good agreement was achieved in heat flux, pressure and shear stress distribution plots. However, there is a concave region near shoulder of opt. geom. 3, similar to opt. geom. 1. And the distribution plots deviate in this region like as they do in the first case (Figure 8 and Figure 10). This deviation validates the comment made about the scope of snapshot pool.

On the other hand, slighter concave region of opt. geom. 3 relative to opt. geom. 1 (Figure 8 a and Figure 10 a) provides itself be inside of the scope of snapshot pool. Consequently, the error percentages were remained at the acceptable levels (Table 5).

Table 6: Validation of case 4 maximizing volume on tabulated results (Opt. Geom. 4)

METHOD	PRES. FORCE (N)	SHEAR FORCE (N)	TOT. DRAG FORCE (N)	MAX. HEAT FLUX (W/m²)	TOT. HEAT ENERGY (W)	VOLUME (m³)
POD-RBF	727.91	48.33	776.24	4302083	1374997	0.14519
DS2Vfiltered	727.94	48.29	776.22	4308100	1373604	0.14519
% ERROR	0.004	0.083	0.003	0.140	0.101	-

a) Optimized geometry

b) Heat flux distribution validation

15
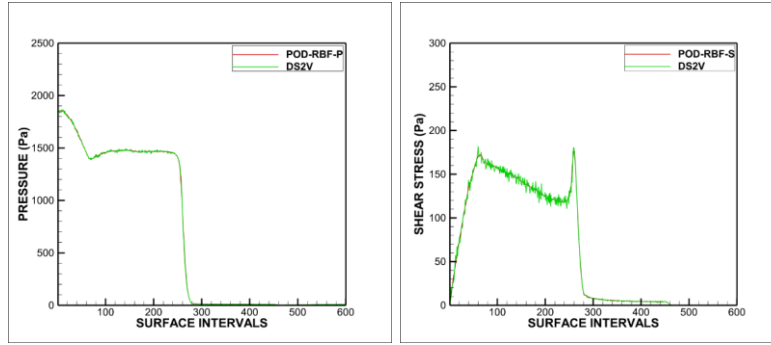
c) Pressure distribution validation d) Shear stress distribution validation
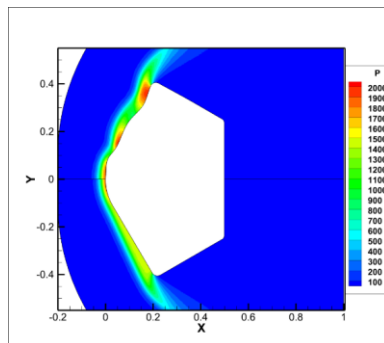Figure 11: Case 4 maximizing volume optimization results validation (Opt. Geom. 4)

In the fourth case, objective function was changed to maximization of the volume while the Stardust re-entry's max heat flux, total heating energy and total drag force values were defined as the constraint functions. However, under these conditions there was not a change in the shape of the geometry (Figure 11 a). In addition to this, having the same geometry solution in the snapshot pool provided an excellent approximation accuracy of ROM model. The agreement quality can be seen from Figure 11 b, c and d and also from Table 6.

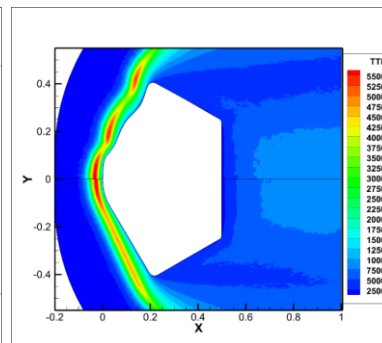## 6.2   Comparison of Stardust and Optimized Geometries

In this section, the optimized geometries' DS2V results were compared with the Stardust re-entry's DS2V results. Pressure and translational contours of optimized geometries were plotted in mirrored form with Stardust (Figure 12 to Figure 14 a and b). Pressure, heat flux and shear stress distributions of both Stardust and optimized geometries were also plotted in the same graphs for comparison (Figure 12 to Figure 14 c, d and e). And their integrated values were also given in tables (Table 7 to Table 9). Objective and constraint functions were indicated on the tables. Fourth case was not given due to having the same geometry with the Stardust re-entry. The noisy distributions were filtered with MATLAB curve fitting tool before integration.

Table 7: Tabulated results of Stardust and Opt. geom. 1

GEOMETRY	PRES. FORCE(N)	SHEAR FORCE(N)	TOT. DRAG FORCE(N) OBJ. FUNC. (max.)	MAX. HEAT FLUX(W/m^2) CONST.	TOT. HEAT ENERGY(W) CONST.	VOLUME (m^3) CONST.
STARDUST	727.94	48.29	776.22	4308100	1373604	0.14519
OPT.GEOM.1	774.20	36.49	810.69	4050300	1273461	0.14483

a) Pressure contours   b) Translational temperature contours

16

c) Pressure distribution   d) Shear stress distribution
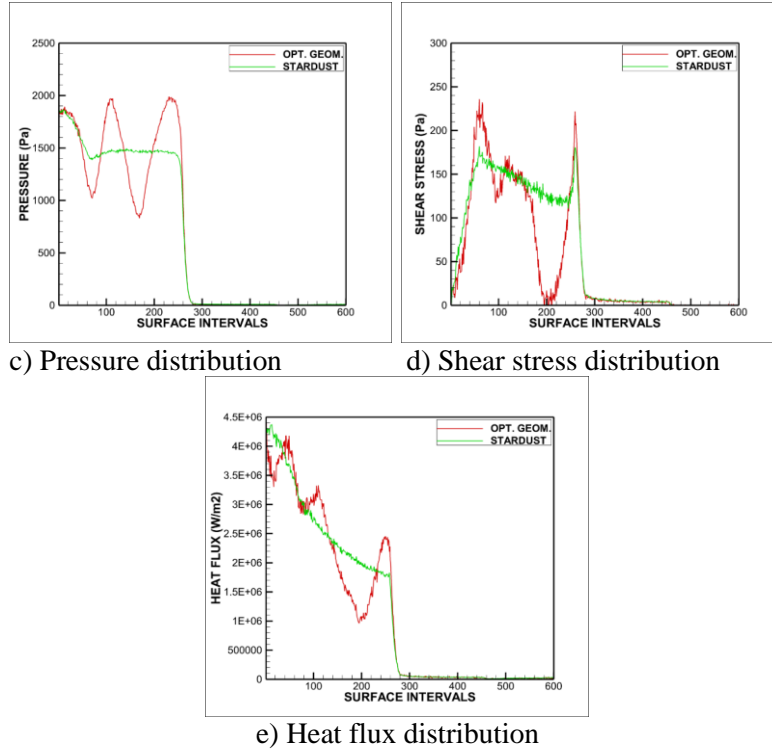

e) Heat flux distribution

Figure 12: Comparison of Stardust and Opt. geom. 1

By aiming the maximization of drag force, Opt. geom. 1 was found. Constraints and the objective function were indicated on the Table 7. The drag force was increased, maximum heat flux and total heating energy were decreased, and the volume was preserved.

According to Figure 12 a and b, the shock core is split into three regions, due to wavy front surface. It is realizable from Figure 12 a, c and d that, concavities increase pressure and decrease shear stress dramatically. In Figure 12 c, these increments can be seen from the second and third peaks. Similarly, sudden decrements in the shear stress can be seen over the same intervals in Figure 12 d.

Due to stagnation points at the nose and at the concave regions, pressure distribution makes peaks (Figure 12 c). Inversely, shear stress makes opposite peaks at the stagnation points (Figure 12 d). Considering the inverse relation between flow speed and pressure, and the expression of shear stress ($\tau = \mu \frac{du}{dy}$), the relation between pressure and shear stress can be understood clearly. Since the flow speed increases while passing over convexities and, decreases while passing over concavities, sudden increments and decrements occur in pressure and shear stress distribution plots (Figure 12 c and d).

On the other hand, by the help of blunter nose, thermal shock core is slightly pushed further (Figure 12 b) in comparison with Stardust's. This results the lower maximum heat flux value at the nose of the geometry (Figure 12 e and Table 7). Wavy surface of the geometry causes splitting at the shock core (Figure 12 b). And these split shock cores preserve the high temperature in their core (red regions in Figure 12 b). These high temperature effects cause the peaks in the heat flux distribution (Figure 12 e). However, despite these peaks, thermal shock cores are located far from geometry surface and as a result, the total heating energy is reduced (Table 7).

Table 8: Tabulated results of Stardust and Opt. geom. 2

GEOMETRY	PRES. FORCE(N)	SHEAR FORCE(N)	TOT. DRAG FORCE(N) CONST.	MAX. HEAT FLUX(W/m²) CONST.	TOT. HEAT ENERGY(W) OBJ. FUNC. (min.)	VOLUME (m³) CONST.
STARDUST	727.94	48.29	776.22	4308100	1373604	0.14519
OPT.GEOM.2	738.43	37.75	776.19	4316500	1245550	0.14561

a) Pressure contours b) Translational temperature contours

c) Pressure distribution d) Shear stress distribution
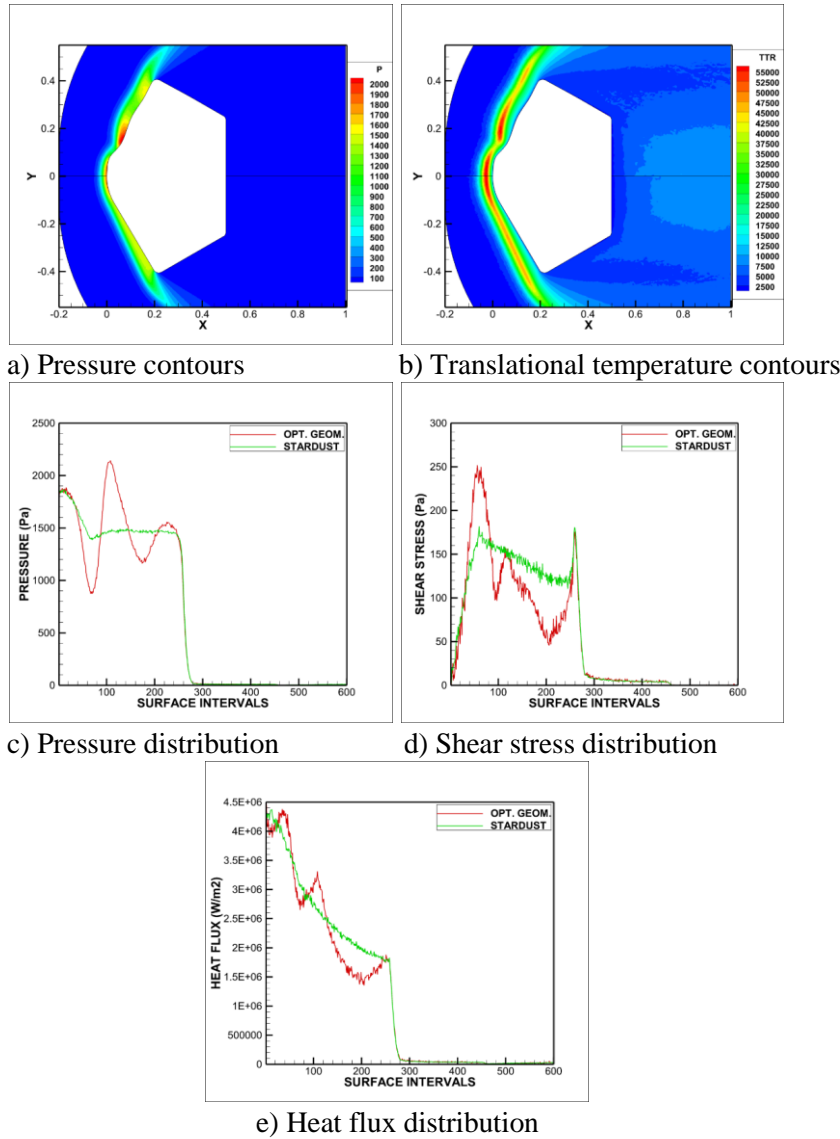

e) Heat flux distribution

Figure 13: Comparison of Stardust and Opt. geom. 2

In the second optimization case, the objective function was changed to minimization of total heating energy while constraining the drag, maximum heat flux and volume. At the end of the optimization, Opt. geom. 2 was found. Total drag force, maximum heat flux value and volume were preserved, total heating energy was decreased.

Similar to Opt. geom. 1, wavy surface was obtained. Therefore, the distribution graphs were obtained as similar to Opt. geom. 1's (Figure 12-13 c, d and e). However, the concavity of the Opt. geom. 2's surface near shoulder region is slighter than Opt. geom. 1's. This causes lower pressure values over there (Figure 13 a), in other words the red region disappears (Figure 12-13 a). So, the resulting drag force is not as high as the Opt. geom. 1's (Table 7 and Table 8). Besides, Opt. geom. 2's blunt nose height is shorter than Opt. geom. 1's. Thus, the thermal shock core cannot be pushed further that much (Figure 12 b and Figure 13 b). Therefore, the maximum heat flux value is not reduced as much as it is in Opt. geom. 1 (Table 7 and 8).

Table 9: Tabulated results of Stardust and Opt. geom. 3

GEOMETRY	PRES. FORCE(N)	SHEAR FORCE(N)	TOT. DRAG FORCE(N) CONST.	MAX. HEAT FLUX(W/m²) OBJ. FUNC. (min.)	TOT. HEAT ENERGY(W) CONST.	VOLUME (m³) CONST.
STARDUST	727.94	48.29	776.22	4308100	1373604	0.14519
OPT.GEOM.3	719.18	47.19	766.37	3680700	1358001	0.14532

| a) Pressure contours | b) Translational temperature contours |

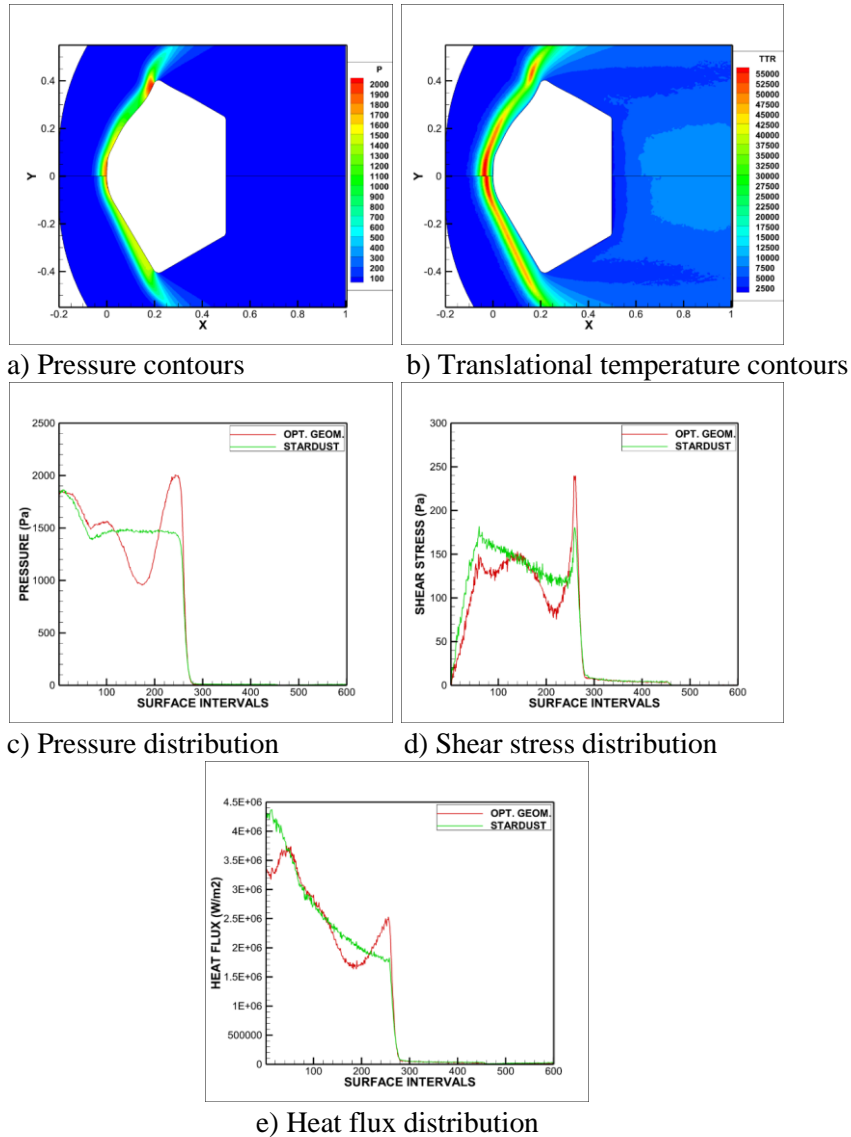| c) Pressure distribution | d) Shear stress distribution |

e) Heat flux distribution

Figure 14: Comparison of Stardust and Opt. geom. 3

In the third case, the objective function was changed to minimization of maximum heat flux. The total drag, heating energy and volume was constrained to the values of Stardust. At the end of the optimization, Opt. geom. 3 was found. Total heating energy and volume were preserved, and maximum heat flux value was decreased. Total drag was also supposed to be preserved but it decreased a bit. According to the POD-RBF result, it was preserved (Table 5 and Table 9). However, an acceptable disagreement was found between DS2V and POD-RBF results.

Being different than the other two cases, optimized geometry was found in convex form except the region close to shoulder. By the effect of dominant convexity, the thermal shock core is pushed further significantly (Figure 14 b). Thus, significant decrement can be achieved in maximum heat flux value (Table 9). At the same time, convexity also decreases the pressure as stated before, however this decrement is balanced with concavity which is close to shoulder region (Figure 14 a).

The similarity of the pressure and shear stress distributions (Figure 14 c and d) between Opt. geom. 3 and Stardust, are the result of having similar nose regions (Figure 14 a). Supportively, pressure and shear distribution plots show the same trend up to 100th interval (Figure 14 c and d). They both have blunt noses and have flatty regions after turning the corner. The flatty region similarity can also be seen from heat flux plot (Figure 14 e) between 50th and 150th intervals. The difference up to 50th interval is sourced by the relatively blunter nose of Opt. geom. 3.

7   Conclusion

In this study, two dimensional aerothermodynamic shape optimization study were conducted on Stardust re-entry in near continuum regime. One of the trajectory point was chosen and axisymmetric calculations were conducted. Design of experiment was designated arbitrarily and developed step by step. Cubic B-spline curves were utilized in the geometry parameterization innovatively. Thus, the number of design variables was able to be reduced, and curve fitting cancelled. Two dimensional axisymmetric DSMC solver [1] was utilized as the physics solver, and flow variable distribution (pressure, shear stress and heat flux) results along the geometry, were implemented in the trained POD-RBF network. In this manner, success of trained POD-RBF network was investigated on hypersonic flow conditions.

Extrapolation capability of the method was found as successful and can provide almost excellent agreement with the simulation results if the prospective geometry is in the scope of the snapshot pool. Despite arbitrarily sampled snapshot pool, the method's extrapolation accuracy shows that it is an appropriate method while reducing the orders of highly nonlinear hypersonic flows. The extrapolation accuracy can be developed further by means of sampling methods (e.g. Latin Hypercube sampling) while forming the design of experiment and it may be the subject of the future works.

References

[1]   Bird, G.A., *The DSMC Method*, CreateSpace, An Amazon Company, 2013

[2]   Lofthouse, A.J., "Nonequilibrium Hypersonic Aerothermodynamics Using the Direct Simulation Monte Carlo and Navier-Stokes Models," Ph.D. Dissertation, Aerospace Engineering Dept., The University of Michigan, Michigan, 2008

[3]   Bird, G.A., *Molecular Gas Dynamics and the Direct Simulation of Gas Flows*, Clarendon Press, Oxford, 1995

[4]   Boyd, I.D., Trumble, K.A. and Wright, M.J., "Modeling of Stardust Entry at High Altitude, Part 1: Flowfield Analysis," *Journal of Spacecraft and Rockets*, Vol. 47, No. 5, September-October 2010
        doi: 10.2514/1.37360

[5]   Ozawa, T., Levin, D.A., Nompelis, I., Barnhardt, M. and Candler, G.V., "Particle and Continuum Method Comparison of a High-Altitude, Extreme-Mach-Number Reentry Flow," *Journal of Thermophysics and Heat Transfer*, Vol. 24, No. 2, April-June 2010
        doi: 10.2514/1.42624

[6]   Bird, G.A., "Nonequilibrium Radiation During Re-entry at 10 km/s," *AIAA 22nd Thermophysics Conference*, AIAA, Honolulu, Hawaii, June 8-10, 1987

[7]   Farbar, E.D., Boyd, I.D. and Martin, A., "Modeling Ablation of Charring Heat Shield Materials for Non-Continuum Hypersonic Flow," *50th AIAA Aerospace Sciences Meeting including the New Horizons Forum and Aerospace Exposition*, AIAA, Nashville, Tenesse, January 9-12, 2012

[8]   Boyd, I.D., Trumble, K. and Wright, M.J., "Nonequilibrium Particle and Continuum Analyses of Stardust Entry for Near-Continuum Conditions," *39th AIAA Thermophysics Conference*, AIAA, Miami, Florida, June 25-28, 2007

[9]   Ozawa, T., Zhong, J., Levin, D.A., Boger, D. and Wright, M., "Modeling of the Stardust Reentry Flows with Ionization in DSMC," *45th AIAA Aerospace Sciences Meeting and Exhibit*, AIAA, Reno, Nevada, January 8-11, 2007

[10]   Schilders, W.H.A., van der Vorst, H.A. and Rommes, J., *Model Order Reduction-Theory Research Aspects and Applications*, Springer-Verlag, Berlin Heidelberg, 2008

[11]   Moreno, A.I., Jarzabek, A.A., Perales, J.M. and Vega, J.M., "Aerodynamic Database Reconstruction via Gappy High Order Singular Value Decomposition," *Aerospace Science and Technology*, Vol. 52, 2016, pp. 115-128
        doi: http://dx.doi.org/10.1016/j.ast.2016.02.004

[12]   Bui-Thanh, T., Damodaran, M. and Willcox, K., "Aerodynamic Data Reconstruction and Inverse Design Using Proper Orthogonal Decomposition," *AIAA Journal*, Vol. 42, No. 8, August 2004

[13]   Bui-Thanh, T., Damodaran, M. and Willcox K. "Proper Orthogonal Decomposition Extensions for Parametric Applications in Transonic Aerodynamics"

[14]   Li, J. and Zhang, W., "The Performance of Proper Orthogonal Decomposition in Discontinuous Flows," *Theoretical & Applied Mechanics Letters*, Vol. 6, 2016, pp. 236-243
doi: http://dx.doi.org/10.1016/j.taml.2016.08.008

[15]   Luo, J., "Design Optimization of the Last Stage of a 4.5-Stage Compressor Using a POD Based Hybrid Model," *Aerospace Science and Technology*, Vol. 76, May 2018, pp. 303-314.
doi: https://doi.org/10.1016/j.ast.2018.01.043

[16]   Luo, J., Zhu, Y., Tang, X. and Liu, F., "Flow Reconstructions and Aerodynamic Shape Optimization of Turbomachinary Blades by POD Based Hybrid Models," *Science China Technological Sciences*, Vol. 60, No. 11, November 2017, pp. 1658-1673
doi: 10.1007/s11431-016-9093-y

[17]   Walton, S., Hassan, O. and Morgan, K., "Reduced Order Modeling for Unsteady Fluid Flow Using Proper Orthogonal Decomposition and Radial Basis Functions," *Applied Mathematical Modeling*, Vol. 37, 2013, pp. 8930-8945
doi: http://dx.doi.org/10.1016/j.apm.2013.04.025

[18]   Xin, C., Li, L., Teng, L. and Zhenjiang, Y., "A Reduced Order Aerothermodynamic Modeling Framework for Hypersonic Vehicles Based on Surrogate and POD," *Chinese Journal of Aeronautics*, Vol. 29, No. 5, 2015, pp. 1328-1342
doi: http://dx.doi.org/10.1016/j.cja.2015.06.024

[19]   Rogers, C.A., Kassab, A.J., Divo, E.A., Ostrowski, Z. and Bialecki R.A., "An Inverse POD-RBF Network Approach to Parameter Estimation in Mechanics," *Inverse Problems in Science and Engineering*, Vol. 20, No. 5, July 2012, pp. 749-767
doi: http://dx.doi.org/10.1080/17415977.2012.693080

[20]   Benaissa, B., Köppen, M., Abdel Wahab, M. and Khatir, S., "Application of Proper Orthogonal Decomposition and Radial Basis Functions for Crack Size Estimation Using Particle Swarm Optimization," *Journal of Physics: Conf. Series*, Vol. 842, 2017
doi: 10.1088/1742-6596/842/1/012014

[21]   Kato, H. and Funazaki, K., "POD-Driven Adaptive Sampling for Efficient Surrogate Modeling and Its Application to Supersonic Turbine Optimization," *Proceedings of ASME Turbo Expo 2014: Turbine Technical Conference and Exposition*, GT2014, Düsseldorf, Germany, June 16-20, 2014

[22]   G. N. Vanderplaats and S. R. Hansen. DOT Users Manual: Version 2.04B. Vanderplaats, Miura Associates, Inc., 1990

[23]   Rogers, D.F. and Adams, J.A., *Mathematical Elements for Computer Graphics*, 2nd ed., Mc Graw-Hill, Inc., USA, 1990

[24]   Sirovich, L., "Turbulence and the Dynamics of Coherent Structures, I-III," *Q. Appl. Math.*, vol. 45, no. 3, pp. 561–571, 1987.

[25]   Forrester, A.I.J., Sobester, A. and Keane, A.J., *Engineering Design via Surrogate Modeling-A Practical Guide*, Wiley, 2008

[26]   Eyi, S. and Yumuşak, M., "Aerothermodynamic Shape Optimization of Hypersonic Blunt Bodies," *Engineering Optimization*, Vol. 47, No. 7, 2015, pp. 909-926
doi: http://dx.doi.org/10.1080/0305215X.2014.933822